The impact of processing on the optical absorption onset of CdTe thin-films and solar cells

Cite as: J. Appl. Phys. 129, 165302 (2021); https://doi.org/10.1063/5.0033415 Submitted: 15 October 2020 . Accepted: 25 March 2021 . Published Online: 27 April 2021

J. J. Andrews, M. Beaudoin, 📵 S. K. O'Leary, 📵 P. Koirala, B. Ramanujam, X. Tan, 📵 M. A. Razooqi Alaani, P. Pradhan, N. J. Podraza, and R. W. Collins







ARTICLES YOU MAY BE INTERESTED IN

Fast mobility induced self-lubrication at metallic glass surface

Journal of Applied Physics 129, 165303 (2021); https://doi.org/10.1063/5.0042222

Hot electron physics and applications

Journal of Applied Physics 129, 150401 (2021); https://doi.org/10.1063/5.0050796

Phase evolution during annealing of low-temperature co-evaporated precursors for CZTSe solar cell absorbers

Journal of Applied Physics 129, 153104 (2021); https://doi.org/10.1063/5.0041320





The impact of processing on the optical absorption onset of CdTe thin-films and solar cells

Cite as: J. Appl. Phys. **129**, 165302 (2021); doi: 10.1063/5.0033415 Submitted: 15 October 2020 · Accepted: 25 March 2021 · Published Online: 27 April 2021







J. J. Andrews,^{1,2} M. Beaudoin,³ S. K. O'Leary,^{1,a)} D. Koirala,^{4,5} D. B. Ramanujam,^{4,5} X. Tan,^{4,5} M. A. Razooqi Alaani,^{4,5} D. P. Pradhan,^{4,5} N. J. Podraza,^{4,5} and R. W. Collins^{4,5}

AFFILIATIONS

- ¹School of Engineering, The University of British Columbia Okanagan, 3333 University Way, VIV IV7 Kelowna, British Columbia, Canada
- ²Advanced Materials and Process Engineering Laboratory, The University of British Columbia, 2355 East Mall, V6T 1Z4 Vancouver, British Columbia, Canada
- ³Stewart Blusson Quantum Matter Institute, The University of British Columbia, 2355 East Mall, V6T 1Z4 Vancouver, British Columbia, Canada
- Department of Physics and Astronomy, The University of Toledo, 2801 W. Bancroft Street, Toledo, Ohio 43606, USA
- ⁵Wright Center for Photovoltaics Innovation and Commercialization, The University of Toledo, 2600 Dorr Street, Toledo, Ohio 43607, USA

ABSTRACT

We critically examine how two processing steps commonly applied in the preparation of cadmium telluride (CdTe)-based solar cells, i.e., the cadmium chloride treatment and the subsequent stepwise bromine/methanol wet etching process, impact the structural and optical properties of polycrystalline CdTe thin-films. In particular, drawing upon a conjuncture of photothermal deflection spectroscopy and spectroscopic ellipsometry experimental results, we determine the spectral dependence of the optical absorption coefficient, $\alpha(E)$, over the photon energy range from 1.1 to 2.0 eV for samples of rf sputtered (RFS) and close space sublimation (CSS) CdTe. The impact of these processing steps on shaping the grazing incidence x-ray diffraction pattern is also examined. We extend the analysis to devices through interpretation of the spectral dependence of the external quantum efficiency associated with two cadmium chloride treated CdTe-based solar cells. The cells are comparably prepared with the exception of the absorber, one by RFS and the other by CSS. Through the use of our results for the thin-film CdTe optical functions and a model for the solar cell multilayer structure, we simulate the resultant external quantum efficiency spectrum. Through a critical contrast with the corresponding solar cell acquired experimental results, we glean insights into the carrier trapping and recombination processes that occur within the two types of CdTe absorbers.

Published under an exclusive license by AIP Publishing. https://doi.org/10.1063/5.0033415

I. INTRODUCTION

Polycrystalline cadmium telluride (CdTe) is currently viewed as one of the dominant thin-film material technologies for commercialized photovoltaic (PV) device applications. Thin-film solar cells fabricated from this material offer conversion efficiencies ranging from 18% to 22%. ^{1–5} While these efficiencies are approaching those of the highest performance bulk crystalline silicon solar cells, CdTe prepared in thin-film form allows for lower manufacturing costs and shorter energy payback times. ⁶ In fact, CdTe-based PV technology has achieved one of the lowest levelized costs

of electricity among all energy sources as well as state-of-the-art field stability. Thus, CdTe-based PV offers a conjuncture of performance and economic advantages when contrasted with other available PV technologies.

In the late 1980s, the cadmium chloride (CdCl₂) treatment of thin-film CdTe-based solar cells was identified and patented as a critical step whereby the conversion efficiency of such cells could be enhanced.⁸ The CdCl₂ treatment significantly improves the performance of solar cell devices by inducing re-crystallization and grain coalescence of the polycrystalline CdTe.^{8–12} A preferential Cl

a)Author to whom correspondence should be addressed: stephen.oleary@ubc.ca

concentration at grain boundaries has also been hypothesized to passivate local non-radiative recombination centers. ^{11,12} This post-deposition treatment involves annealing CdTe thin-film-based materials and solar cell structures between 350 and 450 °C for up to 60 min under a CdCl₂ ambient at atmospheric pressure. ^{10,11} Initial studies have focused on the role that the CdCl₂ treatment plays in increasing the grain sizes associated with the CdTe crystal-lites, ^{9,10} and more recent modeling by Mukherjee *et al.* ¹³ has been applied to explore the effects of the grain size distribution on device performance. Metzger *et al.* ¹⁴ have emphasized the strong influence that this processing step exerts on the underlying defect chemistry of CdTe and the passivation of grain boundaries that are present within these solar cell absorbers.

In addition to the $CdCl_2$ treatment, which modifies the properties in the bulk of the CdTe absorber, other treatments have been applied to modify the CdTe surface for optimal back contact formation. Studies of single crystal CdTe have demonstrated that a stepwise bromine/methanol (Br₂/MeOH) wet etching process, varying from 1 to 0.05 vol.% Br₂ in MeOH, leads to a ~0.4 nm amorphous Te (a-Te) layer on the surface of the crystal. Such treatments have been applied to polycrystalline CdTe in solar cells following the CdCl₂ treatment. Establishing a Te-rich surface has served as the first step in the formation of Cu_x Te back contacts for high efficiency CdTe solar cells. This etch has also been shown to mildly passivate the CdTe surface; however, when it is too aggressive a detrimental Te-rich region with a high recombination velocity forms at the surface.

In this research, we seek to determine how these processing steps used in the preparation of CdTe-based solar cells, i.e., the CdCl₂ treatment and the subsequent Br₂/MeOH wet etching process, influence the structural and optical properties of polycrystalline CdTe thin-film samples fabricated by rf sputtering (RFS) and close space sublimation (CSS). Accordingly, the role that these processing steps play in modifying the film structure, as determined from the grazing incidence x-ray diffraction (GIXRD) pattern, is examined. Then by combining photothermal deflection spectroscopy (PDS) and spectroscopic ellipsometry (SE) experimental results for the same set of samples, we determine the spectral dependence of the optical absorption coefficient, $\alpha(E)$, over the photon energy range from 1.1 to 2.0 eV, spanning the 1.5 eV bandgap of CdTe. We particularly focus this investigation on the transition between the subgap and supergap regions of the spectrum in $\alpha(E)$, with the aim of resolving the form of the Urbach tail. The SE measurement is also used to determine the spectral dependence of the supergap $\alpha(E)$ and full-range refractive index, n(E). In order to complete the analysis, we measure the spectral dependence of the external quantum efficiency (EQE) associated with two different CdCl2 treated and comparably prepared CdTe-based solar cells, one with an absorber prepared by RFS deposition and the other being prepared by CSS deposition. Using our CdTe thin-film optical function results, i.e., $\alpha(E)$ and n(E), based on a structural model for the solar cell, we simulate the resultant EQE spectrum. By considering the difference between the simulation and the solar cell acquired experimental results, we obtain insights into the carrier trapping and recombination processes that occur within RFS and CSS CdTe absorbers.

This paper is organized in the following manner. In Sec. II, the experimental methods applied in this study are presented. Then, the results acquired from the experimental measurements are featured in

Sec. III, with further analysis and discussion stemming from these results being detailed in Sec. IV. The EQE spectral results, corresponding to measurements performed on the CdTe-based solar cells, are then shown in Sec. V; further details, related to the associated EQE simulations, are provided in the Appendix. Finally, the conclusions of this study are drawn in Sec. VI.

II. EXPERIMENTAL METHODS

A. Materials fabrication and structural characterization

Polycrystalline CdTe thin-film samples $2 \mu m$ thick were grown by two different methods, RFS and CSS, on uncoated vitreous silica substrates for analysis by structural and optical measurements. The RFS CdTe thin-films were deposited at a growth temperature of 250 °C. The area of the CdTe sputtering target is $12.7 \times 38.1 \text{ cm}^2$. The rf target power, Ar flow, and deposition pressure were set at 200 W, 23 stand. cm³/min (sccm), and 10 mTorr, respectively. The CSS prepared CdTe thin-films were deposited in a home-built reactor, as described previously. 17,18 The source material was CdTe powder placed in a graphite crucible. The substrates were supported by a second graphite plate kept in close proximity to the source material. The graphite plates were heated independently using tungsten-halogen lamps. All CSS thin-films were deposited in an ambient consisting of He. During CSS growth, the substrate temperature was held between 550 and 610 °C and the source temperature was held in the range from 620 to 680 °C.

Following the depositions on fused silica, two identically prepared sets of RFS thin-film structures, indicated as RFS₁ and RFS₂, and one set of CSS thin-film structures were examined in detail. Each of these three sets of structures was subsequently divided into three subsets in order to study the effect of the two surface treatments. For each set of structures, one member of the subset was left untreated, i.e., as-grown, one was subjected to CdCl2 treatment only, and one was subjected to CdCl2 treatment and subsequently etched using 0.05 vol.% Br₂/MeOH. The CdCl₂ treatment was performed by coating the CdTe surface with a saturated solution of CdCl2 in MeOH and then the structure was annealed at 390 °C for 30 min in a dry air ambient. No delamination was observed upon treatment and the CdCl₂ treated CdTe samples were cleaned with a MeOH rinse. Real time SE was applied to characterize the subsequent Br₂/MeOH etching process and to identify conditions for mild passivation using the instrumentation described in Sec. II C. 15,19,20 This process led to a surface characterized by a stable roughness layer with a 1.2 nm a-Te layer covering the surface. In this stable surface condition, approximately 35 nm of bulk CdTe is removed in a single etch step.

GIXRD was used in order to evaluate the effects of the post-deposition treatments on the crystallite orientation. The GIXRD scans were collected with a Philips XPert Pro MRD system equipped with a hybrid 4-bounce high intensity monochromator using the line focus mode of a Cu $K_{\alpha I}$ source $(\lambda=0.1506\,\text{nm}).$

B. Solar cell fabrication and characterization

Heterojunction solar cells were fabricated using RFS n-type CdS window layers and p-type CdTe absorber layers, the latter grown by either RFS or CSS in depositions separate from those used for the materials fabrication on vitreous silica. A standard

superstrate configuration for the solar cells was used with the light entering through commercial SnO₂:F coated soda lime glass (SLG) (TEC-15M; Pilkington, NA). Four coatings are applied to the SLG by the glass manufacturer, yielding the multilayer structure SLG/SnO₂/SiO₂/SnO₂:F/SnO₂. The ~330 nm thick SnO₂:F is the transparent conducting oxide front contact and the adjoining ~100 nm SnO₂ is a high resistivity transparent (HRT) layer designed to reduce shunting. The RFS 60–120 nm thick CdS layer is followed by a $2\,\mu\mathrm{m}$ thick layer for the RFS CdTe absorber and a 4–5 $\,\mu\mathrm{m}$ thick layer for the CSS CdTe absorber. The optimal processes used for the absorber layers in the solar cells are similar to those used for the materials fabricated on vitreous silica for the GIXRD and PDS measurements.

After the absorber layer deposition, the as-grown solar cells were CdCl₂ treated under the same conditions as the thin-films and then transferred to a thermal evaporator for deposition of standard Cu/Au (4/40 nm) back contacts. For the solar cells, no Br₂/MeOH etching was applied before the back contact deposition. The devices with back contacts 0.08-0.125 cm² in area were annealed at 150 °C for 45 min in an air ambient for Cu diffusion. The completed solar cells were characterized by EQE measurements at room temperature using a commercial instrument (PV Measurements, Inc.). The efficiency of the RFS CdTe solar cell was 12.3% with a V_{OC} value of 0.815 V and a fill-factor of 0.702 and that of the CSS solar cell was 14.8% with a V_{OC} value of 0.826 V and a fill-factor of 0.736. ¹⁸ These performance parameters are representative of the optimum absorber layer processes developed independently for the RFS and CSS deposition methods on TEC-15M type glass. As indicated here, when all processes other than the absorber layer are the same in solar cell fabrication, the optimized CSS solar cells have systematically higher $V_{\rm OC}$ and fill-factor than the RFS solar cells.

C. Optical characterization

Although transmittance measurements of the $2-5\,\mu m$ thick CdTe absorber layers used in solar cells provide suitable sensitivity to $\alpha(E)$ in the photon energy range of the Urbach tail, such films can exhibit considerable surface roughness and associated light scattering, leading to challenges in data interpretation and low accuracy. As a result, PDS, which provides $\alpha(E)$ through the sample heating that occurs upon absorption of incident photons, has been valuable in this application. PDS was used as described elsewhere in order to study the optical absorption spectrum near and below the CdTe bandgap. The measurements were performed over the spectral range of $1100-700\,\mathrm{nm}$, i.e., photon energies between $1.13\,\mathrm{and}\,1.77\,\mathrm{eV}$, in $2\,\mathrm{nm}$ steps.

In mirage effect PDS, a modulated monochromatic light source, at normal incidence to the sample surface, is used as the pump beam. The pump beam is incident on the thin-film CdTe side of the film/substrate sample. When the pump beam is absorbed, it creates periodic heating in the sample which causes a temperature gradient, $d\Theta/dx$, in the medium immediately in front of the sample. By choosing a liquid medium whose refractive index is sensitive to temperature, i.e., $dn/d\Theta$ is large, a modulated refractive index gradient is induced near the sample surface. We chose CCl₄ for the purposes of this study as it satisfies this requirement and, as a result, is a commonly employed liquid in PDS studies. A

laser probe beam passing through this refractive index gradient, grazing the surface of the sample on the film side, will be deflected by an angle, Φ , which depends strongly on the amount of absorption that occurs within the sample. This is how the PDS approach allows for the acquisition of the optical absorption spectrum.

Our PDS setup uses a quartz tungsten-halogen lamp for the pump beam (150 W), a 0.5 m f/4 monochromator, and a position sensitive detector (UDTR®) with a home-built pre-amplifier whose output is fed into a lock-in amplifier. All data presented were collected using a lock-in technique at a chopper frequency of 8 Hz. In PDS, since the signal depends on the thermal response in addition to the optical response, 23-26 higher chopper frequencies yield information closer to the sample surface whereas lower frequencies yield information deeper within the sample. In practical terms, higher frequencies tend to improve the PDS signal-to-noise ratio while reducing the absolute magnitude of the signal. For the 8 Hz frequency used in our experiments, the signal derives from the entire CdTe thickness. The probe beam is sourced from a 4 mW, 632 nm HeNe laser focused to a waist size of less than 15 µm in grazing incidence in front of the sample. The CdTe samples were cut into pieces 1 mm wide (the PDS interaction length) and 8 mm long. The data sets were collected using LABVIEW software. Normalization is achieved by dividing the raw PDS spectra with a PDS spectrum collected from a 1 mm wide sample of polished graphite. Graphite was selected for calibration due to its strong absorption and nearly photon energy independent optical response. Each spectrum is normalized to its corresponding saturation value.

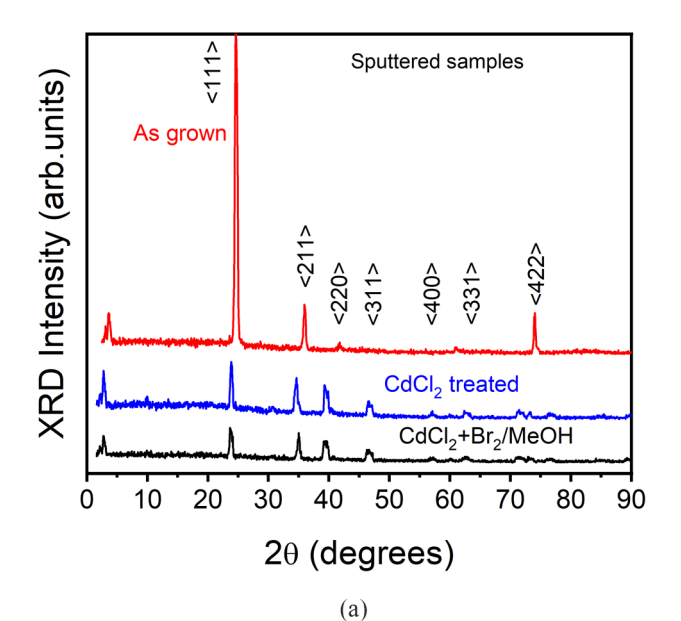
SE measurements of as-grown and CdCl₂ treated RFS were performed using a commercial high-speed multichannel spectroscopic ellipsometer (J.A. Woollam Co., Inc, Model M2000) in the rotating compensator configuration. The measurements on the as-grown sample were performed *in situ* after deposition and after cooling the sample to room temperature, but before opening the chamber to the ambient. Measurements after CdCl₂ treatment were performed *ex situ*. In both cases, surface roughness overlayer corrections were performed in order to extract the complex dielectric function spectra of the bulk CdTe layer. ^{15,19,28}

III. RESULTS

A. Effect of deposition and treatments on CdTe polycrystalline structure

From the GIXRD measurements, all CdTe thin-films are observed to be polycrystalline. The as-grown RFS materials exhibit a strong preferred $\langle 111 \rangle$ orientation, as shown in Fig. 1(a), whereas the as-grown CSS materials are randomly oriented but with a much weaker preference for $\langle 111 \rangle$, as shown in Fig. 1(b).

The GIXRD scans for the RFS material presented in Fig. 1(a) show a large reduction in the intensity of the $\langle 111 \rangle$ peak after CdCl₂ treatment and the appearance, or increased intensity, of the $\langle 220 \rangle$, $\langle 311 \rangle$, $\langle 400 \rangle$, and $\langle 331 \rangle$ peaks, which are weak or not observed before treatment. In contrast, the $\langle 211 \rangle$ and $\langle 422 \rangle$ peaks are unaffected or suppressed. It can therefore be concluded that CdCl₂ treatment of the RFS samples breaks the preferred $\langle 111 \rangle$ orientation for these materials, as seen in Fig. 1(a) and as has been previously reported. In addition to breaking the preferred orientation, the CdCl₂ treated sample, as well as the CdCl₂ treated and



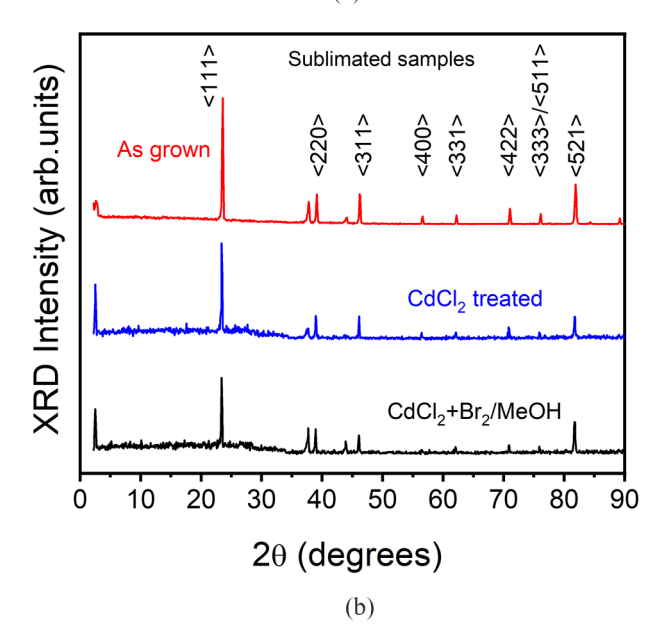


FIG. 1. GIXRD spectra of (a) the RFS CdTe thin-films and (b) the CSS CdTe thin-films, both in the three states: as-grown, CdCl₂ treated, and CdCl₂ treated and Br₂/MeOH etched. When the sputtered films are treated with CdCl₂, the (111) peak intensity is dramatically reduced and other peaks appear, indicating re-crystallization to a randomly oriented polycrystalline film. Post-deposition treatment does not appear to change the orientation of the CSS film. The online version is depicted in color.

subsequently Br₂/MeOH etched sample, also display shifts in the peak positions which indicate that the as-grown RFS films are strained and that the post-deposition CdCl₂ treatment relaxes the strain. Subsequent etching of the CdCl₂ treated samples with Br₂/MeOH is not observed to further alter the crystallite orientations.

For the CSS CdTe materials, the crystal orientation remains mostly independent of sample bulk and surface treatments, as is shown in Fig. 1(b). The peaks appearing at smaller angles adjacent to the $\langle 220 \rangle$ and $\langle 311 \rangle$ peaks for the CSS sample are attributed to surface TeO2. This phase arises because the CSS CdTe is cooled from high temperature under a flow of He with a relatively high concentration of residual gases compared to the RFS CdTe which is cooled from a much lower temperature under high vacuum. No evidence of Te precipitates in any of the samples is observed. The broader XRD peaks for the RFS samples in general reflect a smaller grain size. Scanning and transmission electron microscopy of the CdCl2 treated RFS absorbers in solar cells reveals an average grain size of $\sim\!\!0.3\,\mu\mathrm{m}$, whereas the grains of the CSS absorbers are typically an order of magnitude larger at $\sim\!\!3\,\mu\mathrm{m}$. 18,21

B. Optical absorption by PDS and SE

The PDS analysis of Rosencwaig and Gersho²⁹ for a single thin-film provides the theoretical basis underlying this measurement technique. Fernelius²⁶ expanded upon this analysis to include two layers having different thermal and optical properties. Chan and Beaudoin²⁴ further refined these analyzes to include multiple light reflections within the sample and its coating. Through the solution of a series of one-dimensional heat equations, one can obtain an expression for the PDS signal as a direct function of the optical absorption coefficient, α , of the thin-film. This yields sets of complex coupled equations that are calculated using MATLAB[®] code.²⁴

For the special case that the thin-film is thermally thin, i.e., that the temperature is essentially constant across the thin-film, and that multiple reflections of light within the thin-film are ignored, the Rosencwaig–Gersho expression can be approximated to extract α directly and easily, ³⁰, i.e.,

$$\alpha = -\frac{1}{l} \ln \left(1 - \frac{S}{S_{sat}} \right), \tag{1}$$

where S is the PDS signal at a given photon energy, S_{sat} is the PDS signal at saturation, and l is the thickness of the thin-film. This is often referred to as the Amer and Jackson approximation for α (the Amer–Jackson α). Amer and Jackson³⁰ assert that their approximation is valid within $\pm 20\%$, as long as the thin-films are thermally thin. As will be shown below, this approximation to the Rosencwaig–Gersho expression is actually much better than $\pm 20\%$.

Figure 2 shows an example of fits to the normalized PDS spectra based on the Amer–Jackson α , with the data shown by the open circles. The first simulated spectrum is generated using the original Rosencwaig–Gersho model that neglects multiple reflections within the thin-film and is shown by the red line. This is achieved by inserting the Amer–Jackson α into the Rosencwaig–Gersho expression. This simulated spectrum almost reproduces the observed PDS data, as evidenced by the two insets of Fig. 2. This demonstrates that the Amer–Jackson α reproduces the Rosencwaig–Gersho expression to better than 0.05% at all energies below the PDS saturation. The second simulated spectrum, shown by the blue line, is generated by inserting the Amer–Jackson α into the Chan–Beaudoin extension to the Rosencwaig–Gersho model that takes into account the multiple reflections

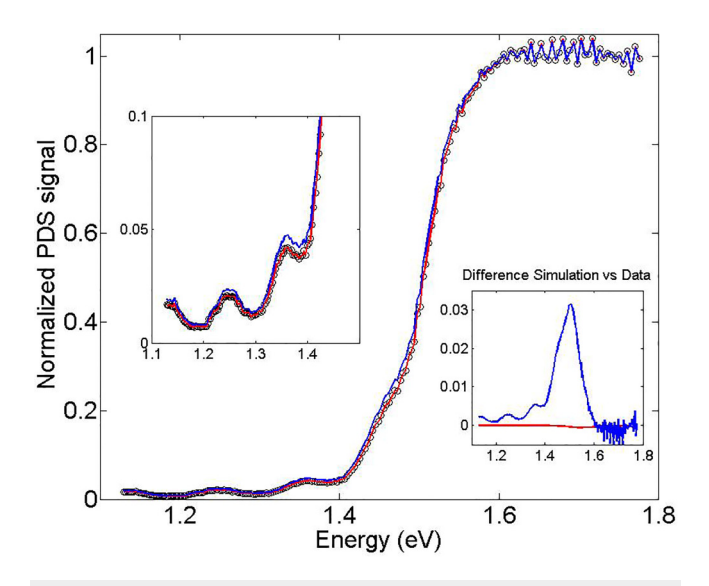
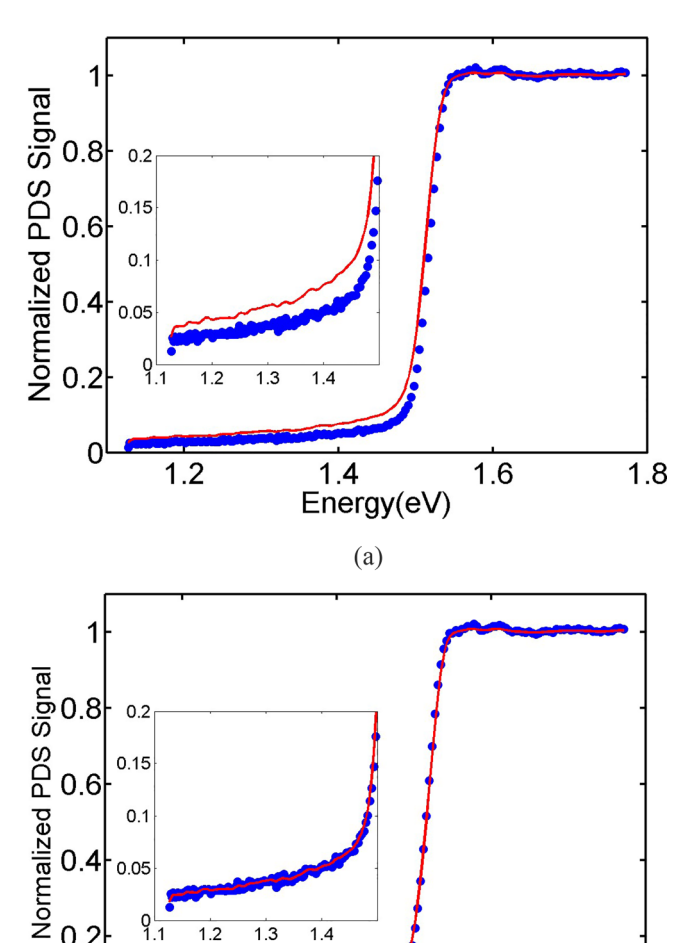


FIG. 2. The PDS spectrum is shown by the open black circles for an as-grown CdTe thin-film prepared by rf sputtering. A simulated spectrum, shown by the solid red line, is generated by introducing $\alpha(E)$ obtained through the Amer and Jackson approximation into the original Rosencwaig-Gersho expression. The solid blue line is simulated by introducing the same $\alpha(E)$ but into the Rosencwaig-Gersho expression extended by Chan and Beaudoin to account for multiple reflections. The online version is depicted in color.

within the thin-film. In this simulation, both the front and backside reflectivities of the CdTe thin-film (both assumed to have refractive indices of $n_1 = 2.98$), sandwiched between glass and CCl_4 (refractive indices of $n_2 = 1.46$), are 0.12 as determined from the usual expression $R = \left| (n_1 - n_2)/(n_1 + n_2) \right|^2$. This shows that neglecting multiple reflections in the simulations for this sample leads to a 3% overestimation of the PDS signal. As shown in our previous work on GaAs-based thin-films, 23,25 the effect is even more pronounced for different thin-film reflectivities, such as can be the case for textured or rough thin-films. Taking multiple reflection effects into account leads to lower values for the optical absorption coefficient, i.e., the multiple passes that occur lead to an enhanced "overall" absorbance and thus an enhanced PDS signal. To reproduce the PDS spectrum with the full model therefore demands that the estimate to the α value be reduced.

The PDS spectra of all samples are analyzed using the extended model that takes into account multiple reflections within the thin-films. Equation (1) is used to provide an initial estimate of the optical absorption spectrum. Then, it is found that the estimate to the α value can be reduced in the unsaturated region to yield results that are consistent with the more complete model. We typically find that a uniform scaling factor is adequate, as illustrated in Fig. 3. In Fig. 3(a), the spectral dependence of the normalized PDS signal associated with an as-grown CSS sample is shown along with simulations using the Amer-Jackson α and the full model with multiple reflections. The simulated normalized PDS signal obtained by this method exceeds that of the experimental results over most of the spectral range (not including the saturation region). We then iteratively re-scaled the optical absorption in the simulation.



Energy(eV) (b) FIG. 3. The PDS spectra for the as-grown CSS CdTe thin-film sample, solid dots, and simulations using (a) $\alpha(E)$ obtained through the Amer-Jackson approximation, and (b) $\alpha(E)$ obtained by our boot-strapping modification of the same approximation. The simulations are shown by the solid lines. The online version is depicted in color.

1.6

1.3

1.2

0.2

This was done until the obtained optical absorption results produced a normalized PDS signal that agreed with the experimental results. We call this a boot-strapping procedure; this procedure was applied to all materials, as it was found that lowering our estimate of the α value by a constant factor was sufficient to yield PDS modeled signal results compliant with those of the experiment. Visual inspection was employed for the purposes of this analysis. The signal calculated by inserting this α value into the full model of Chan and Beaudoin²⁴ is compared with the experimentally obtained PDS curve in Fig. 3(b).

1.8

This boot-strapping procedure was used to deduce the optical absorption spectrum for all materials and is shown in Fig. 4(a) for one set of the RFS materials and in Fig. 4(b) for the CSS materials. Although the procedure itself is a mathematical algorithm, it nevertheless allows one to obtain a more accurate estimate of the material's true optical absorption coefficient. The RFS samples show the effects of thin-film interference fringes in the semi-transparent region of the spectrum. These interference effects are absent in the CSS grown films due to the high roughness that is present at the film growth surface.

Also shown in Figs. 4(a) and 4(b) are the absorption spectra of CdTe materials for photon energies above the bandgap derived from the complex dielectric function obtained by SE. For the RFS materials of Fig. 4(a), the SE measurements were performed on thinner as-grown and CdCl₂ treated materials (\sim 0.1 μ m) deposited on silicon wafers under the same conditions. In Fig. 4(b), the SE

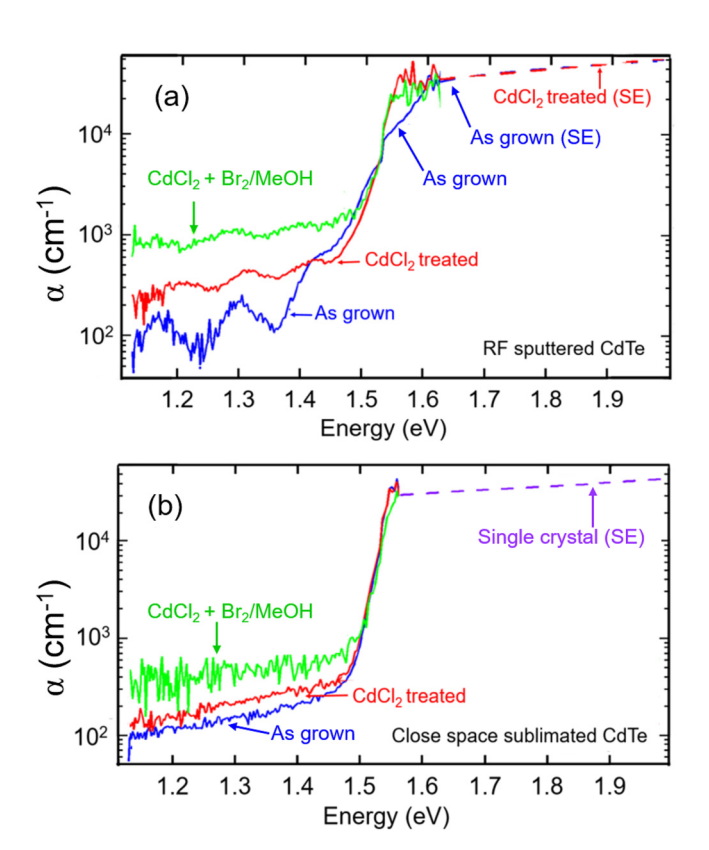


FIG. 4. The optical absorption spectra of CdTe thin-films obtained from PDS measurements using our boot-strapping procedure of the Amer–Jackson approximation for (a) the RFS samples and (b) the CSS samples. The interference fringes in (a) derive from the thickness of the films and are absent from the spectra in (b) due to the surface roughness of the sublimated films. Following each treatment, the subgap absorption determined from PDS increases. Also included are the absorption spectra above the bandgap deduced from SE measurements of the complex dielectric function for (a) as-grown and CdCl₂ treated RFS CdTe and (b) single crystal CdTe (broken lines). The online version is depicted in color.

results were obtained from the smooth surface of single crystal CdTe. Because the thinner films and single crystal CdTe are smoother than the thick films, particularly for those made by CSS, the optical properties are determined more accurately from SE using these materials. In fact, on the scale of Figs. 4(a) and 4(b), all three absorption spectra determined by SE are essentially indistinguishable for the depicted photon energy range above the gap. In addition, at the 1.62 and 1.56 eV transitions between the two data sets in Figs. 4(a) and 4(b), respectively, good agreement between the optical absorption coefficients obtained by PDS and SE is observed.

The acquired optical absorption spectra of Figs. 4(a) and 4(b), plotted on a logarithmic scale vs photon energy, show different behaviors over three ranges: (i) a gradually increasing trend in subgap absorption whereby the starting or ending state of the optical transition is localized well below the band edge; (ii) a steep Urbach tail that represents optical transitions associated with deviations from perfect crystalline periodicity, e.g., electron-phonon interactions in single crystals or static disorder and potential fluctuations due to grain boundaries and stress in the polycrystalline films; and (iii) a second gradually increasing trend due to band-to-band transitions above the bandgap. For both RFS and CSS materials, an increase in the subgap optical absorption is observed when the samples are treated with CdCl2. The subsequent Br₂/MeOH treatment was also found to increase the subgap absorption. For the specific photon energy of 1.2 eV, the subgap absorption within the RFS material increased from 330 to 800 cm⁻¹ with Br₂/MeOH treatment whereas the subgap absorption within the CSS material increased from 140 to 500 cm⁻¹. The origins of this enhanced absorption corresponding to the CdCl₂ and Br₂/MeOH treatments remain unclear at present. In the following, the analysis focuses on the breadth of the Urbach tail for the two materials and the changes that occur with treatment.

IV. ANALYSIS AND DISCUSSION

It is often the case that the spectral dependence of the optical absorption coefficient associated with a semiconductor near its energy gap is characterized in terms of the abruptness with which it is attenuated as it approaches the subgap spectral region. $^{31-34}$ The Urbach tail is a quasi-exponential region of the absorption spectrum vs E just below the bandgap E_g . It can be captured by the following expression: 23,25,34

$$\alpha = \begin{cases} \alpha_t \exp\left(\frac{E - E_t}{E_0}\right) + \alpha_0 & \text{for } E \leq E_t, \\ \alpha_t + \alpha_0 & \text{for } E > E_t, \end{cases}$$
 (2)

where E_t is an optical gap energy identifying the transition between the Urbach tail and the band-to-band absorption regions in the model, $\alpha_t + \alpha_0$ is the absorption coefficient at E_t , E_0 is the Urbach breadth, and α_0 is the assumed underlying constant absorption coefficient, which is usually attributed to gap states and possibly to surface defects.

Traditionally, E_0 and E_t values are extracted by fitting the exponential portion of the absorption edge. E_0 is the slope and E_t is the extrapolated optical gap energy defining the transition in absorption behavior. Another way to extract E_0 and E_t is to use

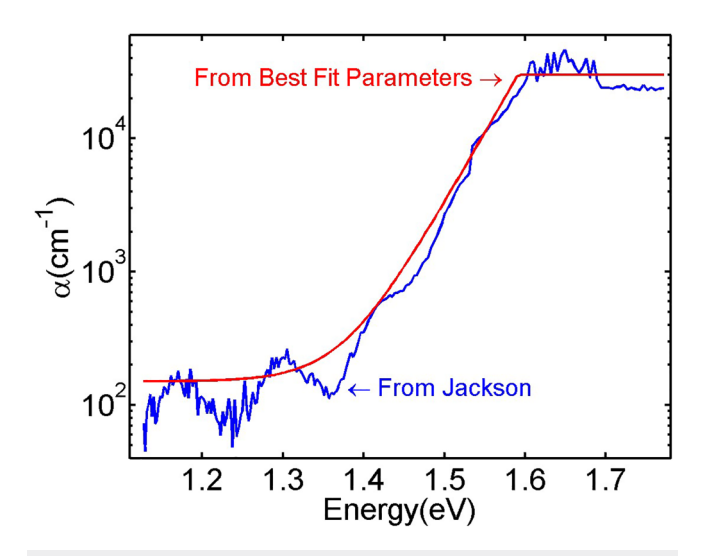


FIG. 5. The optical absorption spectrum for an as-grown RFS CdTe thin-film, obtained from the boot-strapped Amer–Jackson approximation, compared with a simulated spectrum (solid line) using Eq. (2). Good agreement is observed between the two unique methods. The online version is depicted in color.

Eq. (2) as the model absorption spectrum. This model absorption spectrum is inserted into the full simulation, extended for multiple reflections, and a fit to the PDS data allows for the extraction of E_0 , E_b and α_0 . The spectral dependence above the optical gap energy is neglected in the analysis as it can be obtained by other methods. In fact, the spectral dependence of α cannot be determined above E_t using the PDS approach as it occurs in the saturation region. Here, SE measurements can extend the range of $\alpha(E)$ to energies above E_b as is shown in Fig. 4. For the spectral dependence of each normalized PDS signal within the framework of Eq. (2), we determine the values of E_0 , E_b and α_0 that ensure the best fit between the expressions of Chan–Beaudoin^{2,4} and the experimental results; this is performed using MATLAB's Curve Fitting Toolbox.

A representative best-fit optical absorption result, corresponding to an as-grown RFS thin-film, is contrasted with that acquired through our boot-strapping procedure in Fig. 5. The blue line is the absorption spectra obtained from our boot-strapping method whereas the red line is the absorption coefficient according to Eq. (2). This figure shows good agreement between the two methods and validates the use of Eq. (2) for samples where our boot-strapping method would not be possible. This was the case, for instance, in our previous studies of GaAs-based thin-films. ^{23,25} Similar results to those of Fig. 5 are obtained for the other samples in this study.

Since the PDS signal saturates upon full absorption, the exact spectral dependence of the optical absorption coefficient above E_t is unresolvable within the framework of the PDS approach itself for optically thick films. As previously noted, results above E_t can be obtained from SE. The Urbach edge parameters E_0 , transition energies E_t , and gap state absorption constants α_0 for all thin-films subjected to the analysis that applies Eq. (2) are reported in Table I. Figure 6 summarizes the evolution of E_0 with surface treatments for the three sets of samples from Table I.

Also shown in Table I are the most accurately available bandgaps E_{σ} for the CdTe materials obtained by the so-called critical point analysis.^{35,36} This analysis is performed by taking the second derivative of the complex dielectric function spectra as obtained by SE, an alternative method compared to traditional modulation spectroscopy, and fitting the second derivative using a general expression for a bandgap critical point. The differences in bandgap are well understood in terms of in-plane compressive stress in the thin-films, which leads to a wider bandgap.³⁷ Thus, it has been concluded that an important role of the CdCl2 treatment of RFS CdTe is to relax the stress in the thin-film, as also indicated by GIXRD. In fact, the bandgap of the RFS CdTe approaches that of the single crystal after such a treatment. For the CSS CdTe, accurate CP analyses to determine the bandgaps are not possible due to the extensive roughness of the as-grown and CdCl2 treated samples, as well as the residual roughness and the a-Te layer that remain after Br₂/MeOH etching. For this material, due to the high substrate temperature during growth and large grain sizes, 18 the bandgap of this material has been assigned to that of single crystal CdTe in

TABLE I. Optical absorption onset and bandgap values obtained for RFS and CSS CdTe thin-films in three states: as-grown, $CdCl_2$ treated, and $CdCl_2$ treated and $Br_2/MeOH$ etched. "From fit" is extracted as a best-fit parameter when applying the full multiple reflection model to the normalized PDS data. The bandgap E_g is obtained from a critical point analysis of the complex dielectric function obtained by SE. The entry "s.c." indicates E_a from single crystal CdTe.

Sample	E_0 (meV) from fit (±2 meV)	E_t (eV) from fit (±0.003 eV)	$\alpha_0 \text{ (cm}^{-1}) \text{ from}$ fit (±25 cm ⁻¹)	E_g (eV) from SE CP analysis (±0.005 eV)
RFS ₁ (as-grown)	39	1.596	205	1.529
RFS ₁ (CdCl ₂ anneal)	19	1.549	289	1.493
RFS_1 (CdCl ₂ + etch)	25	1.569	1152	
RFS ₂ (as-grown)	41	1.591	151	
RFS ₂ (CdCl ₂ anneal)	21	1.559	470	
RFS_2 (CdCl ₂ + etch)	21	1.558	1366	
CSS (as-grown)	13	1.543	200	1.491 (s.c.)
CSS (CdCl ₂ anneal)	13	1.542	271	
CSS ($CdCl_2 + etch$)	21	1.571	484	

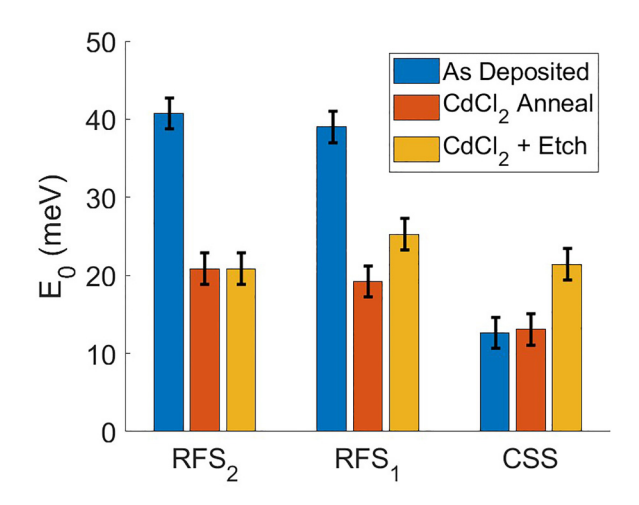


FIG. 6. Urbach breadth parameter E_0 for CdTe thin-films including RFS and CSS samples in three states: as-grown, CdCl₂ treated, and CdCl₂ treated and Br₂/MeOH etched. The numerical values are given in Table I. The results show a sharpening of the absorption edge upon CdCl₂ treatment for the RFS samples. The online version is depicted in color.

Table I determined by the same method as for the thin-films.³⁷ This assignment was made for subsequent interpretations of the relationship between the bandgap and optical gap energies.

Table I shows that both E_t and E_0 decrease for the RFS samples as a result of the CdCl₂ treatment. These values do not seem to change further, however, in response to Br₂/MeOH etching. In contrast, these energies remain relatively constant throughout for the CSS samples, with the exception of the etched sample. As a caveat, however, we note that this particular sample has a rougher surface than the others, thus making it more challenging to obtain accurate PDS spectra. Furthermore, for the polycrystalline CdTe-based thin-films represented in Table I, changes upon Br₂/MeOH etching may be difficult to interpret due to the formation of the a-Te layer on the surface and possibly in surface-connected grain boundary regions as well.

Considering only the CdCl₂ treated samples, as these are relevant for the solar cell structures, it can be concluded that the CSS material exhibits a narrower Urbach breadth, $E_0 = 13$ meV, in comparison with the RFS samples, $E_0 = 20$ meV. These values can be compared with the earlier results for single crystals, i.e., in the range of 7-11 meV, 38-40 as reviewed in Ref. 41. The larger values of E₀ for the RFS materials may account for the consistently lower V_{OC} and fill-factor values for optimized solar cells with RFS absorbers compared with CSS absorbers. A recent model that quantitatively relates the $V_{\rm OC}$ loss due to the E_0 value for a nonabrupt band edge⁴¹ would predict a larger effect (~40 mV) than that observed here (~10 mV); however, other effects may be limiting $V_{\rm OC}$ and the fill-factor for both the RFS and CSS solar cells. Further implications of a broader Urbach tail for the RFS samples are discussed in Sec. V, where the EQE spectrum for the solar cell with the RFS absorber is analyzed.

For all materials, the relationship in Table I between the optical gap energy and the bandgap is given by $E_t = E_g + (E_0/2) + 0.046$ eV.

Additional discussion of the origin of such a relation is warranted. At a similar transition energy, E_t , between the Urbach and band-to-band transitions in hydrogenated amorphous silicon (a-Si:H)-based materials, an approximate condition for continuity of the first derivative of the absorption coefficient is $E_t \approx E_g + 2E_0$, derived using analytical forms for the Urbach tail and the band-to-band transitions. 42,43 As a result, E_t is typically 0.08-0.12 eV above the bandgap E_g as determined by the Cody–Lorentz model for these materials. Differences between the different types of energy gaps of this order were demonstrated for the case of a-Si:H by Sweenor et al., 44 so such differences may also be expected for CdTe as well. In fact, the energy E_t defined in this way for a-Si:H through continuity of the zeroth and first derivatives of $\alpha(E)$ also matches the mobility gap as determined by internal photoemission measurements. The corresponding expression for E_t relevant for a direct bandgap crystalline semiconductor, such as CdTe, can be derived as $E_t = E_g + (E_0/2)$; however, with the relaxation of continuity of the derivative in Eq. (2), the offset of E_t from the bandgap is expected to be larger. Thus, the first two terms of the relationship $E_t = E_g + (E_0/2) + 0.046$ eV would be expected for continuity of the zeroth and first derivative of the Urbach edge and the band-to-band regions. The final constant is then an offset that accounts for the form of Eq. (2), specifically the discontinuity at the transition between the two regions.

V. COMPARISONS WITH EQE OF CdTe SOLAR CELLS

PDS is sensitive to all absorption processes that degrade to heat in the CdTe thin-film material, and thus upon calibration provides $\alpha(E)$. The measured EQE spectrum, however, is only sensitive to those absorption processes in the CdTe that generate free electrons and holes that are collected in the device. As a result, the shape of the optical absorption onset deduced from these two methods can differ, and any observed difference furnishes insight into the carrier trapping and recombination processes that occur within the material being examined.

In order to understand these differences quantitatively, and thereby gain insight into the carrier trapping and recombination processes, we draw upon our CdTe optical function results, i.e., $\alpha(E)$, acquired from a conjuncture of our PDS and SE results, and n(E), acquired from our SE results alone, corresponding to the experimental measurements performed on our polycrystalline thinfilm CdTe samples. Using an SE developed model for the multilayer structure of the solar cell, first assuming all photogenerated electrons and holes within the CdTe are collected and contribute to the EQE, we simulate the spectral dependence of the EQE. The difference between the simulations and the experimental data provides insights into deviations from the assumptions of the model. For CdTe, the dominant deviation arises from the loss of photogenerated carriers by recombination, and iterative changes are made to the model for improved agreement between the EQE simulation results and the experimental data. The changes to the model include varying the fraction of carriers excited within different laminar regions of the absorber that are not collected but instead recombine. Ultimately in this process, a specific collection profile vs depth within the absorber can be identified that results in a simulated EQE spectrum that agrees with the measured spectrum,

within the limits of experimental error. ^{21,46} While in previous work, such an analysis has been performed above the CdTe bandgap, thus far very little attention had been focused on comparisons between the simulated and measured EQE spectrum below the bandgap. We feel that this represents a deficiency in the field that we aim to remedy as an important application of our accurately determined subgap $\alpha(E)$.

We first consider the form of the EQE spectrum for the case of a solar cell incorporating an RFS CdTe absorber layer that is deposited and CdCl₂ treated under identical conditions as the RFS CdTe thin-films studied by GIXRD and PDS, described in Secs. III–IV. The modeling procedure is presented in detail elsewhere and requires the spectral dependence of n(E) and $\alpha(E)$ for all component materials incorporated within the CdTe-based solar cells over the EQE spectral range under examination in this study, i.e., $1.3-4.0 \, \text{eV}$, along with an appropriate structural model for the solar cell itself. A detailed enumeration of the assumptions used in our EQE simulations is provided in the Appendix.

For the thinner components ($<0.5 \mu m$), such as the glass coatings and CdS, SE is an accurate method for extracting both $[n(E), \alpha(E)]$ spectra for use in our EQE modeling. The SE method is applied to single layers deposited on well-characterized substrates or to partial or complete film stacks using analytical models with photon energy independent parameters that describe the component layer $[n(E), \alpha(E)]$ spectra. For the thick components of the cell, such as the SLG substrate (3.2 mm) at the front of the device and the CdTe absorber $(2 \mu m)$, however, a measurement, such as SE, which is based solely on reflection, cannot provide sufficiently accurate spectra for α over the weak absorption range of the absorption onset. For materials such as SLG, with smooth surfaces, accurate values for $\alpha(E) < 10^3$ cm⁻¹ require transmission spectroscopy to supplement the higher α values obtained by SE in the ultraviolet range. For thick layers, such as CdTe with rough surfaces, the application of both SE and transmission spectroscopy to obtain $\alpha(E)$ in the weak absorption range can be challenging. Difficulties exist due to the use of effective medium theories, which are only approximate, and due to light scattering, which can often be neglected in SE but not in transmission spectroscopy. By combining SE analysis results for $[n(E), \alpha(E)]$ of CdTe, where $\alpha(E)$ is obtained near and above the bandgap, with the PDS results for $\alpha(E)$ below the bandgap, then optical properties suitable for solar cell EQE modeling can be generated.

With a full set of optical properties of the components, the solar cell structure, including bulk, surface, and interface roughness layers, can be deduced from a least-squares regression analysis of SE data on the complete solar cell. 21,46 A step-by-step analysis procedure has been applied to evaluate the hierarchy of the critical structural and optical parameters in the regression analysis. This procedure was beneficial because of the complexity of the optical model for the CdTe solar cell, which requires a through-the-glass measurement, including stress-induced birefringence in the SLG, roughness layers at the interfaces, and adjustable parameters in selected component optical properties. 21,46 Adjustments in optical property parameters may be needed due to the thickness and substrate dependencies of $[n(E), \alpha(E)]$ and sample-to-sample variations that arise because the materials that are measured to determine $[n(E), \alpha(E)]$ may differ from those in the actual device.

Figure 7 shows the simulated EQE spectrum for an RFS CdTe-based solar cell, applying the procedure described in the previous paragraphs along with the assumptions outlined in the Appendix. In Fig. 7, we also plot the corresponding experimental EQE spectrum for the RFS fabricated solar cell incorporating a CdCl₂ treated CdTe absorber. Very close agreement between the simulation and the data is observed over the photon energy range from 1.5 to 1.6 eV in Fig. 7, as a result of the selected collection profile described in the Appendix. The data extend slightly above the simulation in a narrow ~0.05 eV range near and below the bandgap, an effect attributed to light trapping, as noted in the Appendix. At energies below the bandgap, the experimental EQE data show exponentially increasing behavior with photon energy characteristic of an Urbach tail. Fitting over the most accurate EQE range of 0.01 < EQE < 0.2 gives an Urbach edge breadth, shown in the figure, of 14.0 ± 0.5 meV.

Thus, the notable observation in Fig. 7 is the steeper slope or smaller E_0 for the Urbach tail of the experimental EQE data compared to the simulation which has a breadth of 20.4 meV, a value reflecting the PDS $\alpha(E)$ of the CdTe absorber. This difference leads to the result that the simulated EQE is larger than the measured EQE at energies less than ~ 1.47 eV. This result in turn indicates that some fraction of the optical excitations starting from or ending at localized states, as reflected in the PDS experimental data, do not result in free carriers that generate current, as reflected in the EQE data. The implication is that the resulting carriers generated by this

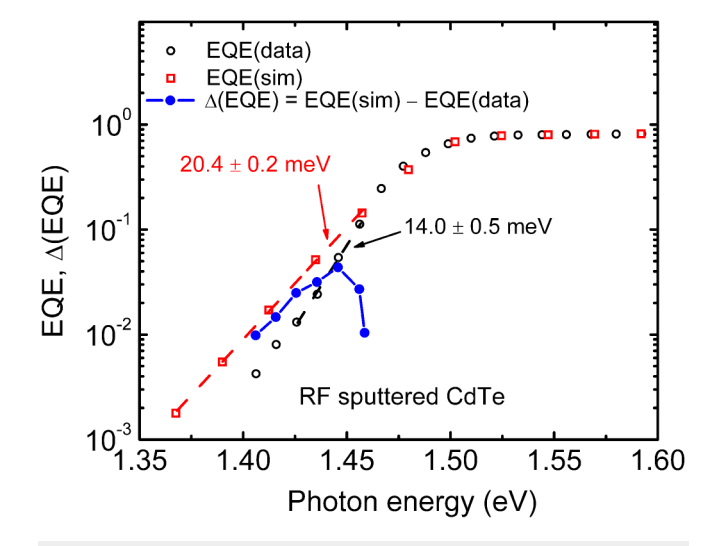


FIG. 7. EQE spectra in the vicinity of the bandgap for a CdCl $_2$ treated CdTe-based solar cell with an absorber layer fabricated by RFS. The spectra are plotted on a logarithmic scale vs photon energy. For the experimental EQE data (open circles), the Urbach breadth E_0 is obtained over the most accurate range of 0.01 < EQE < 0.2. For the EQE simulation (open squares), a linear fit over the range of 0.001 < EQE < 0.2 was performed. The solid line connecting the closed points shows Δ EQE, the difference between the simulated and measured EQE spectra over the range where positive results are obtained, indicating optical excitations from or to localized tail states that do not generate free carriers. The online version is depicted in color.

fraction of excitations recombine. Figure 7 includes the difference between the simulated and measured EQE, which describes recombination loss, and appears as a band approximately 0.03 eV wide that parallels the EQE onset as the energy is reduced and decreases rapidly as the energy is increased above 1.465 eV or 0.028 eV below the bandgap. For the electrons and holes generated through these transitions, it is likely that one carrier is trapped sufficiently deeply such that thermal re-excitation does not occur over the time period of the trapped carrier lifetime and recombination results. In fact, at a photon energy of 1.42 eV or ~70 meV lower than the bandgap, Fig. 7 suggests that most excited carriers recombine.

Figure 8 shows a comparison of the experimental EQE spectra for the solar cells incorporating CdCl₂ treated RFS and CSS CdTe absorbers. Fitting over the most accurate EQE range gives the Urbach breadths shown in the figure, 14.0 ± 0.5 meV for the RFS CdTe solar cell, as in Fig. 7, and 13.4 ± 1.4 meV for the CSS CdTe solar cell. Although this small difference is well within the range of experimental error, measurements of other cells prepared under similar conditions show a consistent ~1-2 meV slope difference. The notable observation that contrasts the CSS CdTe solar cell from the RFS cell, comparing the results in Fig. 8 and Table I, is the agreement between the experimental EQE and Urbach breadth values for the CSS cell. Given that EQE simulations reflect the $\alpha(E)$ Urbach tail of CdTe from PDS, this behavior demonstrates that for the CSS CdTe solar cell no band tail recombination is detected and all carriers generated by Urbach tail excitations are separated and collected. This may occur due to the smaller Urbach tail breadth for the CSS materials and possibly a longer carrier lifetime that allows thermal excitation of carriers trapped in the Urbach edges.

Another difference noted in Fig. 8 is the redshift of the EQE of the CSS CdTe solar cell relative to that of the RFS cell. This shift may occur for three possible reasons. First, the CSS CdTe is

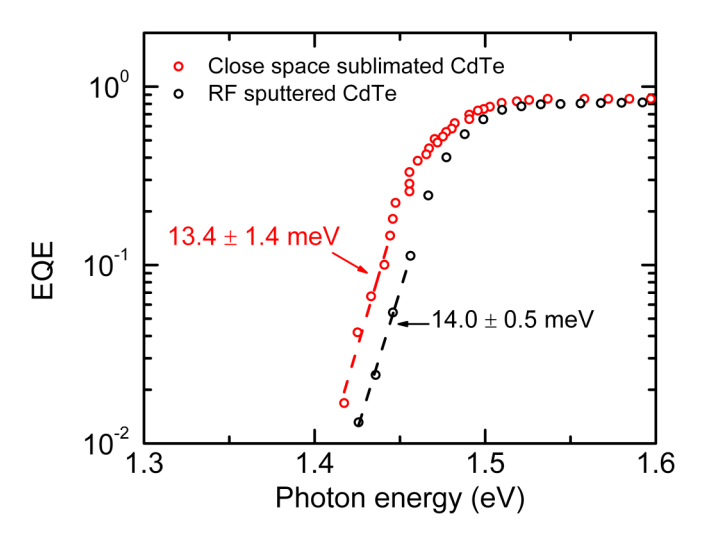


FIG. 8. Experimental EQE spectra for RFS and CSS CdTe-based solar cells. These cells incorporate $CdCl_2$ treated absorber layers fabricated in similar processes as those whose absorption spectra are plotted in Fig. 4. The online version is depicted in color.

typically deposited to greater thicknesses, which allows for collection at lower energies along the absorption onset; second, the rougher back contact interface for the CSS cell allows for enhanced light scattering and trapping in multiple reflections; and third, a reduced in-plane compressive film stress may lead to a bandgap of ~0.002 eV redshifted and close to that of the single crystal for the CSS CdTe. All these effects can give the CSS CdTe solar cell a small increase in short circuit current density relative to the RFS CdTe cell in addition to the additional collection of carriers excited by Urbach tail absorption.

Before concluding this section, we would be remiss not to mention a possible methodological difficulty that underlies our interpretations. It is appropriate to question the validity of applying CdTe optical properties acquired through measurements of thinfilms deposited on vitreous silica substrates in simulations of measurements of CdTe thin-film absorbers deposited on CdS layers in solar cells. In fact, different underlying substrates or layers could lead to differences in the CdTe grain morphology and other such properties. Furthermore, in the preparation of the solar cells, a back contact is applied and a subsequent anneal is performed, which could change the properties of CdTe thin-films in devices. The most compelling argument for the validity of our approach is that our EQE experimental results acquired on a solar cell can be accurately modeled using optical properties acquired on our CdTe thin-films, and the resulting structural model is in agreement with electron microscopy.^{21,46} In addition, the key conclusions of this work are based on observed differences between the RFS and CSS thin-film optical properties and observed similarities between the RFS and CSS solar cell EQE spectra. In this study, it is valid to compare the two different deposition methods for the same underlying material and post-deposition steps. In the future, however, it is critically important to understand more generally the role of substrate and underlying material in the nucleation, growth, structure, and electronic and optical properties of CdTe thin-films.

VI. CONCLUSIONS

We have critically examined how two processing steps commonly used in the preparation of CdTe-based solar cells, i.e., the CdCl₂ treatment and the subsequent Br₂/MeOH wet etching process, affect the structural and optical properties of polycrystalline CdTe thin-film samples fabricated by RFS and CSS. The structural properties have been evaluated through GIXRD and the optical properties have been measured through a combination of PDS and SE. From the latter measurements, we have determined the spectral dependence of the optical absorption coefficient, $\alpha(E)$, for CdTe samples from 1.1 to 2.0 eV, spanning the 1.5 eV bandgap. We have applied the measured optical properties to an analysis of the spectral dependence of the EQE associated with two CdCl₂ treated CdTe-based solar cells comparably prepared with the exception of the absorber, one by RFS and the other by CSS. From a structural model for the solar cell and from component layer optical properties, we simulated the resulting EQE spectrum for the RFS cell. Through a critical comparison with the corresponding solar cell acquired experimental results, we have gained insights into the carrier trapping and recombination processes that occur within the two types of solar cells.

A key observation is that the EQE onset for the CSS CdTebased solar cell has the same Urbach breadth as the PDS-derived result, within the limits of the experimental errors associated with each measurement. As a result, we conclude that all photoexcitations associated with the Urbach tail in this cell generate free carriers that are collected. In contrast, for the RFS CdTe solar cell, the EQE onset has a smaller Urbach breadth than the PDS-derived result, which indicates the presence of a band of excitations that result in carrier recombination. The difference in behaviors is believed to result from the fact that the Urbach tail for the CSS material is narrower and that the trapped carrier lifetime may be longer as well. As a result, photoexcited carriers in localized initial or final states are close enough in energy to the extended states and reside in the localized states longer such that thermal excitation of the localized carriers to the band states occurs followed by carrier collection.

The deeper localized states involved in the optical transitions and Urbach edge recombination in the RFS thin-films and solar cells that are not observed in CSS films and cells are likely to arise from the potential and bandgap fluctuations associated with the grain boundaries and residual stresses in low-temperature deposited RFS thin-films. Although the grain size increases significantly upon CdCl₂ treatment for the RFS materials, the average grain sizes of these materials are still significantly smaller than those of the CSS thin-films ^{18,21} and the associated grain boundaries can contribute to the band tail states. Similarly, residual stresses are also found to be larger in the finer grained material. The more extensive band tail states in the RFS material, and the associated band tail recombination, may account for consistently lower overall performances of the best RFS CdTe-based solar cells compared with the CSS cells. ^{21,47}

AUTHORS' CONTRIBUTIONS

The samples and devices were synthesized and supplied by Koirala and Tan who also performed the EQE measurements. EQE analysis and modeling was performed by Koirala, Pradhan, and Ramanujam. The work at the University of Toledo was directed by Collins and Podraza. The GIXRD and PDS experiments, and most of the related analysis, were carried out by Andrews supervised by O'Leary (PI) and Beaudoin. Assistance on the GIXRD interpretation was provided by Razooqi Alaani and Collins. Andrews, Beaudoin, O'Leary, and Collins wrote the manuscript with input from all authors.

ACKNOWLEDGMENTS

The authors thank Professor J. F. Young of the Stewart Blusson Quantum Matter Institute for use of the laboratory during PDS experiments and useful insights during the data collection phase. This research was undertaken, in part, thanks to funding from the Max Planck-UBC-UTokyo Centre for Quantum Materials and the Canada First Research Excellence Fund, Quantum Materials and Future Technologies Program, and also supported by the Natural Sciences and Engineering Research Council (NSERC) of Canada. The University of Toledo (UT) co-authors thank Dr. Naba Paudel and Professor Yanfa Yan for assistance in the fabrication of CSS CdTe thin-films. The UT co-authors gratefully acknowledge funding support from the National Science

Foundation (NSF), under Grant No. 1711534 and the U.S. Air Force Research Laboratory, Space Vehicles Directorate, under Contract No. FA9453-19-C-1002. The U.S. Government is authorized to reproduce and distribute reprints for Governmental purposes notwithstanding any copyright notation thereon. The views and conclusions contained herein are those of the authors and should not be interpreted as necessarily representing the official policies or endorsements, either expressed or implied, of Air Force Research Laboratory or the U.S. Government.

APPENDIX: MODELING ASSUMPTIONS UNDERLYING OUR EQE SIMULATIONS

In order to simulate the EQE spectra for the rf sputtered (RFS) CdTe solar cell, a number of key assumptions have been made.

- (1) Specularly reflecting (non-scattering) interfaces are assumed using individual interface roughness layers with optical properties given by the Bruggeman effective medium approximation. If this assumption is not accurate, then the neglected light scattering leads to EQE data that exceed the simulation, typically in a narrow range near the bandgap of the CdTe absorber where the path length of the beam is extended by scattering within the $\sim 2\,\mu\mathrm{m}$ thickness of CdTe.
- (2) For close agreement between the supergap EQE simulation and the corresponding measurement, the simulation is based on the assumption of a specific collection profile within the CdTe absorber. In fact, this profile is incorporated to account for a simulation that exceeds the EQE data over a spectral range that depends on where the recombination occurs. For the simulation in Fig. 7, it is assumed that all photons absorbed within the CdS/CdTe interface roughness layer generate electrons and holes that are separated and collected (100% collection). For the front 1.8 μm of the CdTe absorber, it is assumed that 99% of the electrons and holes are separated and collected, whereas only 30% collection is possible from the 0.18 μm region adjacent to the back contact.^{21,46} Such assumptions are required in order to fit the measured EQE spectrum over the range from 1.5 to 4.0 eV (825–310 nm).
- The model incorporates $[n(E), \alpha(E)]$ spectra for CdTe that combine SE results for α above 1.502 eV with PDS results such as those of Fig. 5 below 1.502 eV. Here, the Urbach slope E_0 is taken as an average of the values in Table I for the two RFS materials, which were both processed under the same conditions. The transition photon energy of 1.502 eV, which is within 0.001 eV of $E_g + (E_0/2)$, is chosen so that the derivative of the PDS-derived results is equal to the derivative of the SE-derived results. In addition, the PDS-derived results for α are renormalized to the SE $\alpha(E)$ results at 1.502 eV. Renormalization can avoid discontinuities in α at 1.502 eV, although these discontinuities are small considering the close agreement in Fig. 4(a) between the SE- and PDS-derived results. This implies that the initial normalization with polished graphite is quite accurate. Application of the PDS $\alpha(E)$ results below 1.502 eV is based on the assumption that all optical transitions associated with the Urbach edge absorption lead to electrons and holes that are separated and collected. When this assumption is made, then the Urbach breadth

- associated with the EQE simulation matches the Urbach breadth from PDS, reflecting the dominant spectral dependence of the CdTe $\alpha(E)$ in the EQE simulation in the Urbach edge region. If the assumption of complete collection is not valid due to photogenerated electron and hole recombination, then the EQE simulation will exceed the EQE data within the photon energy range of the Urbach edge.
- (4) Only the Urbach edge component of Eq. (2) is used in the EQE simulation as it is assumed that excitations of carriers represented by α_0 in Eq. (2) start or end on localized states that are sufficiently deep such that free carriers cannot be generated to contribute to the EQE. As noted, this Urbach edge component from PDS dominates the shape of the onset of the EQE in the simulation when it is assumed that all optical transitions associated with the Urbach edge absorption lead to electrons and holes that are separated and collected.

DATA AVAILABILITY

The data that support the findings of this study are available from the corresponding author upon reasonable request.

REFERENCES

- ¹M. Green, E. Dunlop, J. Hohl-Ebinger, M. Yoshita, N. Kopidakis, and X. Hao, Prog. Photovoltaics 29, 3 (2021).
- ²See https://investor.firstsolar.com/news/press-release-details/2016/First-Solar-Achieves-Yet-Another-Cell-Conversion-Efficiency-World-Record/default.aspx for "First Solar Achieves Yet Another Cell Conversion Efficiency World Record," First Solar Press Release (23 February 2016).
- ³M. Gloeckler, I. Sankin, and Z. Zhao, IEEE J. Photovoltaics 3, 1389 (2013).
- ⁴J. Sites, A. Munshi, J. Kephart, D. Swanson, and W. S. Sampath, in *Proceedings* of the 2016 IEEE 43rd Photovoltaics Specialists Conference (PVSC) (IEEE, New York, NY, 2016), p. 3632.
- ⁵W. K. Metzger, S. Grover, D. Lu, E. Colegrove, J. Moseley, C. L. Perkins, X. Li, R. Mallick, W. Zhang, R. Malik, J. Kephart, C.-S. Jiang, D. Kuciauskas, D. S. Albin, M. M. Al-Jassim, G. Xiong, and M. Gloeckler, Nat. Energy 4, 837 (2019).
- ⁶K. P. Bhandari, J. M. Collier, R. J. Ellingson, and D. S. Apul, Renew. Sustain. Energy Rev. 47, 133 (2015).
- ⁷N. Strevel, L. Trippel, C. Kotarba, and I. Khan, Photovoltaics Int. 22, 66 (2013).
- ⁸P. Meyers, C. Leng, and T. Frey, U.S. patent 4,710,589A (1 December 1987). ⁹B. E. McCandless, L. V. Moulton, and R. W. Birkmire, Prog. Photovoltaics 5,
- $^{f 10}$ B. E. McCandless and J. R. Sites, "Cadmium telluride solar cells," in ${\it Handbook}$
- of Photovoltaic Science and Engineering, edited by A. Luque and S. Hegedus (John Wiley & Sons, New York, NY, 2003), p. 617.

 11 For a review, see I. M. Dharmadasa, Coatings 4, 282 (2014).
- 12C. Li, Y. Wu, J. Poplawsky, T. J. Pennycook, N. Paudel, W. Yin, S. J. Haigh, M. P. Oxley, A. R. Lupini, M. Al-Jassim, S. J. Pennycook, and Y. Yan, Phys. Rev. Lett. 112, 156103 (2014).
- 13S. Mukherjee, S. Farid, M. A. Stroscio, and M. Dutta, International Workshop on Computational Electronics (IEEE, New York, 2015), pp. 1-4.

 14W. K. Metzger, D. Albin, M. J. Romero, P. Dippo, and M. Young, J. Appl.
- Phys. 99, 103703 (2006).
- 15D. E. Aspnes and H. Arwin, J. Vac. Sci. Technol., A 2, 1309 (1984).
- ¹⁶M. O. Reese, C. L. Perkins, J. M. Burst, S. Farrell, T. M. Barnes, S. W. Johnston, D. Kuciauskas, T. A. Gessert, and W. K. Metzger, J. Appl. Phys. 118, 155305 (2015).
- ¹⁷C. S. Ferekides, D. Marinskiy, V. Viswanathan, B. Tetali, V. Palekis, P. Selvaraj, and D. L. Morel, Thin Solid Films 361-362, 520 (2000).

- ¹⁸N. R. Paudel and Y. Yan, Thin Solid Films **549**, 30 (2013).
- ¹⁹D. E. Aspnes, Thin Solid Films 571, 334 (2014).
- ${\bf ^{20}}{\rm J.}$ Chen, "Spectroscopic ellipsometry studies of II-VI semiconductor materials and solar cells," Ph.D. dissertation (The University of Toledo, Toledo, OH, 2010), p. 60.
- ²¹P. Koirala, J. Li, H. P. Yoon, P. Aryal, S. Marsillac, A. A. Rockett, N. J. Podraza, and R. W. Collins, Prog. Photovoltaics 24, 1055 (2016).
- ²²M. M. Junda, C. R. Grice, P. Uprety, P. Koirala, R. W. Collins, Y. Yan, and N. J. Podraza, in Proceedings of the 2018 IEEE 7th World Conference on Photovoltaic Energy Conversion (WCPEC) (IEEE, New York, 2018), p. 1902.
- ²³M. Beaudoin, I. C. W. Chan, D. Beaton, M. Elouneg-Jamroz, T. Tiedje, M. Whitwick, E. C. Young, J. F. Young, and N. Zangenberg, J. Cryst. Growth 311, 1662 (2009).
- ²⁴I. C. W. Chan and M. Beaudoin, J. Appl. Phys. **106**, 103510 (2009).
- 25_{M.} Beaudoin, R. B. Lewis, J. J. Andrews, V. Bahrami-Yekta, M. Masnadi-Shirazi, S. K. O'Leary, and T. Tiedje, J. Cryst. Growth 425, 245 (2015).
- ²⁶N. C. Fernelius, J. Appl. Phys. **51**, 650 (1980).
- ²⁷R. W. Collins, "Measurement technique of ellipsometry," in *Spectroscopic* Ellipsometry for Photovoltaics, Fundamental Principles and Solar Cell Characterization, edited by H. Fujiwara and R. W. Collins (Springer Nature, Cham, 2018), Vol. 1, Chap. 2, pp. 19-58.
- 28P. Koirala, J. Li, N. J. Podraza, and R. W. Collins, "Real time and mapping spectroscopic ellipsometry for CdTe photovoltaics," in Spectroscopic Ellipsometry for Photovoltaics, Fundamental Principles and Solar Cell Characterization, edited by H. Fujiwara and R. W. Collins (Springer Nature, Cham, 2018), Vol. 1, Chap. 13, pp. 357-413.
- ²⁹A. Rosencwaig and A. Gersho, J. Appl. Phys. **47**, 64 (1976).
- 30 N. M. Amer and W. B. Jackson, "Optical properties of defect states in a-Si:H," in Semiconductors and Semimetals, edited by J. I. Pankove (Academic, Montreal, 1984), Vol. 21B.
- ³¹F. Urbach, Phys. Rev. **92**, 1324 (1953).
- ³²W. Martienssen, J. Phys. Chem. Solids 2, 257 (1957).
- 33G. D. Cody, "The optical absorption edge of a-Si:H," in Semiconductors and Semimetals, edited by J. I. Pankove (Academic, Montreal, 1984), Vol. 21B.
- ³⁴M. Beaudoin, A. J. G. DeVries, S. R. Johnson, H. Laman, and T. Tiedje, Appl. Phys. Lett. 70, 3540 (1997).
- 35 D. E. Aspnes, "Modulation spectroscopy/electric field effects on the dielectric functions of semiconductors," in Handbook of Semiconductors, Optical Properties of Solids, edited by M. Balkanski (North-Holland, Amsterdam, 1980), Vol. 2, Chap. 4A. $^{\bf 36}$ R. W. Collins and A. S. Ferlauto, "Optical physics of materials," in Handbookof Ellipsometry, edited by H. G. Tompkins and E. A. Irene (William Andrew,
- Norwich, NY, 2005), pp. 93. 37 J. Li, J. Chen, and R. W. Collins, Appl. Phys. Lett. 99, 061905 (2011).
- ³⁸D. T. F. Marple, Phys. Rev. **150**, 728 (1966).
- ³⁹J. L. Sculfort, R. Triboulet, and P. Lemasson, J. Electrochem. Soc. 131, 209 (1984).
- 40 J. T. Mullins, J. Carles, and A. W. Brinkman, J. Appl. Phys. 81, 6374 (1997).
- ⁴¹J. Wong, S. T. Omelchenko, and H. A. Atwater, ACS Energy Lett. 6, 52 (2021).
- 42S. K. O'Leary, S. R. Johnson, and P. K. Lim, J. Appl. Phys. 82, 3334 (1997).
- ⁴³A. S. Ferlauto, G. M. Ferreira, J. M. Pearce, C. R. Wronski, R. W. Collins, X. Deng, and G. Ganguly, J. Appl. Phys. 92, 2424 (2002).
- ⁴⁴D. E. Sweenor, S. K. O'Leary, and B. E. Foutz, Solid State Commun. 110, 281 (1999).
- 45 R. M. Dawson, Y. M. Li, M. Gunes, D. Heller, S. Nag, R. W. Collins, C. R. Wronski, M. Bennett, and Y. M. Li, Proc. MRS 258, 595 (1992).
- 46 P. Koirala, A.-R. A. Ibdah, P. Aryal, P. Pradhan, Z. Huang, N. J. Podraza, S. Marsillac, and R. W. Collins, "Optical simulation of external quantum efficiency spectra," in Spectroscopic Ellipsometry for Photovoltaics, Applications and Optical Data of Solar Cell Materials, edited by H. Fujiwara and R. W. Collins (Springer, Cham, 2018), Vol. 2, Chap. 3, p. 83.
- A. Gupta and A. D. Compaan, Appl. Phys. Lett. 85, 684 (2004).
- 48 H. Fujiwara, J. Koh, P. I. Rovira, and R. W. Collins, Phys. Rev. B 61, 10832 (2000).